Journal of Power Sources 237 (2013) 26–32

Contents lists available at SciVerse ScienceDirect

Journal of Power Sources

journal homepage: www.elsevier.com/locate/jpowsour

Characterization of two phase distribution in electrochemically-lithiated spinel $Li_4Ti_5O_{12}$ secondary particles by electron energy-loss spectroscopy

Mitsunori Kitta*, Tomoki Akita, Shingo Tanaka, Masanori Kohyama

Research Institute for Ubiquitous Energy Devices, National Institute of Advanced Industrial Science and Technology (AIST), 1-8-31 Midorigaoka, Ikeda, Osaka 563-8577, Japan

HIGHLIGHTS

- Distribution of $Li_4Ti_5O_{12}$ and $Li_7Ti_5O_{12}$ phases in a LTO secondary particle was clarified by STEM–EELS.
- Li-inserted $Li_7Ti_5O_{12}$ phases can be clearly identified by Li-*K*, Ti-*L* and O-*K* edge spectra.
- Separated two-phase distribution was observed in a half Li-inserted secondary particle.
- Li-insertion reaction should propagate between primary particles sequentially.

GRAPHICAL ABSTRACT

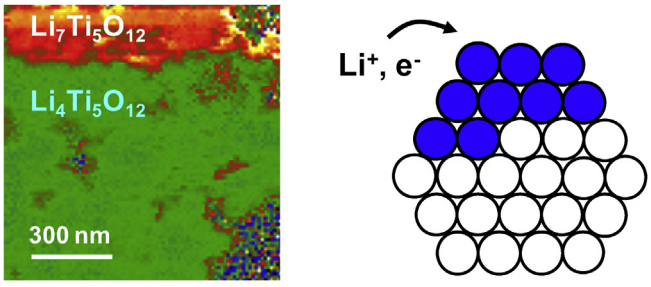

ARTICLE INFO

Article history:
Received 12 February 2013
Received in revised form
28 February 2013
Accepted 5 March 2013
Available online 14 March 2013

Keywords:
Li ion battery
$Li_4Ti_5O_{12}$
Two-phase reaction mechanism
Electron energy loss spectroscopy

ABSTRACT

Spinel lithium titanate, $Li_4Ti_5O_{12}$ (LTO) is attracting much attention as an alternative material replacing carbon based anodes in lithium ion batteries, due to its high rate properties as well as its durability and safety. The coexistence of the two phases, spinel $Li_4Ti_5O_{12}$ and rock salt $Li_7Ti_5O_{12}$, during the charge–discharge reactions is the key issue for the understanding of reaction mechanism and the development of LTO electrodes with improved performance. However, the two-phase distribution morphology in real LTO electrodes has not yet been reported, due to the difficulty in identifying the Li-inserted $Li_7Ti_5O_{12}$ phase with high resolutions. Thus we apply the scanning transmission electron microscopy with electron energy loss spectroscopy (STEM–EELS) using the latest equipment with high energy and spatial resolutions. We have successfully identified the presence of the $Li_7Ti_5O_{12}$ phase in Li-inserted LTO secondary particles, by the EELS analysis of Li composition, Ti oxidation state, and local configurations around oxygen atoms, compared to the $Li_4Ti_5O_{12}$ phase. We have also obtained the two-phase distribution image in 50% Li-inserted LTO secondary particles, where separate presence of both the phases is clearly revealed. This indicates the particle-by-particle reaction mechanism, where the rate determining process exists in the boundary between primary particles.

1. Introduction

Rechargeable lithium ion batteries are used for many portable electric devices such as cell phones and laptop computers as a power source. Recently, many efforts are concentrated on the lithium-ion battery technology for large scale applications such as electric or hybrid electric vehicles and general energy storage equipment for the sake of effective energy utilization and renewable energy collection. There are a lot of technological requirements such as high power, large storage, quick charging, low temperature performance, and especially safety and long life operation. Conventional lithium ion batteries often use carbon or graphite as anode materials. However, due to the low lithium intercalating voltage of approximately 100 mV (vs. Li^+/Li), highly reactive metallic lithium is easily formed under a fast charge rate, and deposited on the surface of electrode particles, leading to a high

* Corresponding author. Tel.: +81 072 751 8703; fax: +81 072 751 9714.
E-mail address: m-kitta@aist.go.jp (M. Kitta).

0378-7753/$ – see front matter © 2013 Elsevier B.V. All rights reserved.
http://dx.doi.org/10.1016/j.jpowsour.2013.03.022

risk of reaction with the electrolyte or charged cathode [1–3]. Therefore, alternative anode materials are highly required for large scale lithium ion batteries. Recently, spinel lithium titanium oxide [4–7] ($Li_4Ti_5O_{12}$, LTO, space group *Fd-3m*) has been focused on as one of the most promising candidates for anode materials of large scale lithium ion batteries, due to its safety under the quick charge–discharge performance as well as long life performance [8,9]. This has been demonstrated by the prototype lithium ion batteries.

This material shows a remarkable constant charge–discharge potential around 1.55 vs Li^+/Li, which suggests a two-phase transition process between $Li_4Ti_5O_{12}$ spinel and $Li_7Ti_5O_{12}$ rock salt according to the general equation proposed as follow [5,7,10]

$$(Li_3)8a(LiTi_5)16d(O_{12})32e + 3Li^+ + 3e^- \rightarrow (Li_6)16c(LiTi_5)16d(O_{12})32e\ldots \quad (1)$$

where the superscripts stand for the number of equivalent sites with Wyckoff symbols for the space group *Fd-3m*. In the electrochemical charge process (defined as Li insertion), additional lithium ions are inserted into octahedral 16c sites, and then all the lithium ions at tetrahedral 8a sites are shifted to 16c sites [7] at the same time. The rigid spinel framework $(LiTi_5)16d\ (O_{12})32e$ provides a three dimensional network of channels for facile lithium diffusion [10] and exhibits an extremely small change in the unit cell volume from $Li_4Ti_5O_{12}$ to $Li_7Ti_5O_{12}$ (less than 0.1%), which leads to the zero strain property [7,11], as excellent stability for high rate charge–discharge performance [9,12].

The charge–discharge reaction mechanism of LTO via the two-phase coexistence state has been investigated by X-ray diffraction [10,13,14] coupled with the maximum entropy method [15], neutron diffraction [16,17], and NMR [16]. However, the coexistence morphology of these two phases, namely $Li_4Ti_5O_{12}$ and $Li_7Ti_5O_{12}$ phases, in usual LTO powder is not yet clear, and the real space observation of it is significantly important in order to understand the detailed process of redox reaction during the two-phase state, leading to the improvement of the basic properties of LTO based electrodes.

In this study, we deal with the two-phase morphology in commercially used LTO powder (LT-106). Fig. 1(a) shows SEM images of the sample powder, which is made of secondary particles, consisting of single crystalline LTO primary particles of 50–100 nm. About the morphology of the two phases in secondary particles, we can expect two types of morphologies derived from different reaction mechanisms. The first is the particle-by-particle reaction as shown in Fig. 1(b), where the Li-insertion reaction extends from a primary particle to a neighboring primary particle sequentially, leading to clearly separated two-phase distribution. In this case, there should be fast reaction diffusion not along the boundary of primary particles but in the primarily particles. The second is the uniform particle reaction as shown in Fig. 1(c), where the reaction proceeds in each primary particle, leading to well-blended two-phase distribution. In this case, there should be fast reaction diffusion along the boundaries between primary particles, compared to the reaction rate inside each primary particle. This is in contrast to the particle-by-particle reaction model.

To investigate which reaction model is adequate, it is desirable to obtain real space images of the two-phase distribution in secondary particles during the reaction. This kind of observation is difficult in usual spectroscopic studies. Even in the TEM, detecting the $Li_7Ti_5O_{12}$ phase inside the $Li_4Ti_5O_{12}$ particle by electron diffraction is not so easy, due to negligible volume change by the Li insertion. Therefore, we adopt the scanning transmission electron microscopy with electron energy loss spectroscopy (STEM–EELS) [18,19]. The STEM–

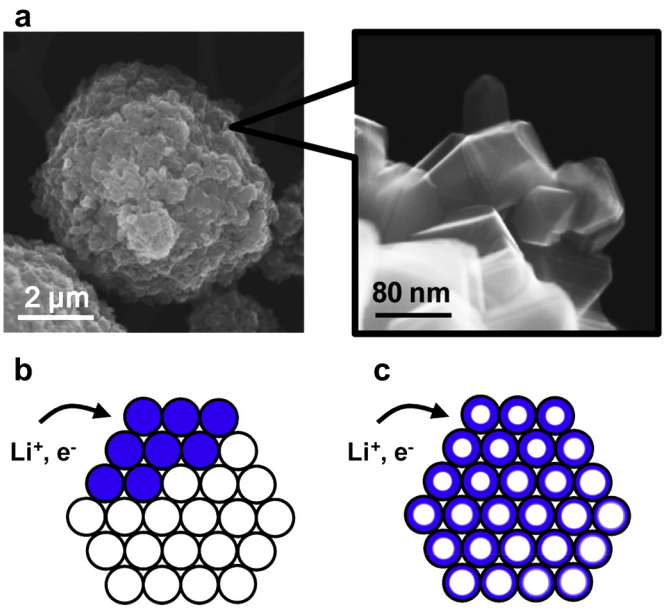

Fig. 1. (a) The micrograph of commercial LTO powder (LT-106) acquired by FE-SEM (S-5500, HITACHI) operated at 30 kV. A secondly particle consists of single-crystalline $Li_4Ti_5O_{12}$ primary particles with sizes of about 50–100 nm. (b), (c) Two types of models of reaction mechanism; particle-by-particle reaction (b) and uniform particle reaction (c). $Li_4Ti_5O_{12}$ and $Li_7Ti_5O_{12}$ phases are shown in white and dark blue colors, respectively. (For interpretation of the references to color in this figure legend, the reader is referred to the web version of this article.)

EELS study using the latest equipment is promising to acquire the image of distribution of chemical composition, oxidation state and electronic structure with high energy and spatial resolutions. Recently, the STEM–EELS spectral imaging has been frequently applied to the visualization of real space distribution of local chemical or electronic states in various materials [20–22]. However, there are no applications to the two-phase distribution in LTO. This should be caused by the lack of detailed characterization of $Li_7Ti_5O_{12}$ generated in $Li_4Ti_5O_{12}$ particles.

In this study, we investigate the morphology and detailed structure of the two-phase coexistence state in LTO secondary particles. For this purpose, first we perform detailed EELS characterization of electrochemical Li-inserted LTO samples so as to examine whether $Li_7Ti_5O_{12}$ phases are really generated or not. Here we show that the EELS analysis of the chemical and electronic states can identify the presence of the $Li_7Ti_5O_{12}$ phase for the first time, while the crystal structure analysis has been used generally [14,17]. Second, based on the obtained EELS data of the $Li_4Ti_5O_{12}$ and $Li_7Ti_5O_{12}$ phases, we examine the two-phase distribution morphology in LTO secondary particles by the STEM–EELS spectrum imaging method so as to clarify the reaction mechanism. In our preceding work [23], we applied the EELS analysis to LTO thin-film samples, made from a TiO_2 wafer [24], to identify surface product layers after the initial Li-insertion and extraction processes. In the present study, we deal with the two-phase distribution in real LTO powder samples during the Li-insertion process for the first time.

2. Materials and methods

Electrochemical lithium-ion intercalation experiments were carried out for commercial LTO ($Li_4Ti_5O_{12}$) powder (LT-106, purchased from Ishihara Sangyo Kaisha, LTD) with metallic lithium as a counter electrode. LTO powder, consisting of secondary particles with about ~6.9 μm of diameter and 10.9 $m^2\ g^{-1}$ of BET, was mounted on a 10 mm Cu-mesh current collector and compressed into a thin sheet as the positive electrode without any conductive

carbon or PTFE binder. The cells were assembled and sealed in a dry air filled box with lithium foil as the anode and 1 M $LiPF_6$ dissolved in EC/DMC (1:1 by volume) as the electrolyte. A galvanostatic Li-insertion experiment (electrochemical charge of $Li_4Ti_5O_{12}$) was performed at about 0.3 C rate for 3 cycles. After the electrochemical charge experiment, the cell was dismantled in a dry air filled box and the sample was rinsed by DMC solution to wash out the electrolyte and other impurities. Then the LTO powder samples were dispersed in DMC solutions and then deposited on 3 mm copper grids coated with a holey amorphous carbon film as a specimen for the TEM analysis.

The prepared specimen was then observed in an analytical TEM (TITAN^{3TM} G2 60-300, FEI Company) operating at 200 kV with a Wien filter monochrometer and equipped with an improved high tension tank and a high resolution GIF (Quantum, GATAN, Inc.). The EELS measurement was performed with the microscope in the STEM mode at a total energy resolution of 0.25 eV determined by the full width at half maximum of the zero-loss peak. The EEL spectra were collected with the 0.05 eV/channel energy dispersion and an integration time $t = 0.01$ s per read out for Li-*K* edge region and $t = 0.05$ s per read out for Ti-*L* and O-*K* edge region. Afterward, the collected spectra were corrected for dark current. For the calibration of energy scale at Li-*K* edge region, the zero-loss peak was measured simultaneously. For the Ti-*L* and O-*K* edge region, the pre peak of the O-*K* edge at 532.5 eV served as fix point for the energy calibration.

3. Results and discussion

3.1. Differences in EEL spectra between $Li_4Ti_5O_{12}$ and Li-inserted $Li_4Ti_5O_{12}$

The $Li_7Ti_5O_{12}$ phase is considered to be formed by electrochemical Li insertion into usual LTO ($Li_4Ti_5O_{12}$) powder. Here we experimentally examine the formation of the $Li_7Ti_5O_{12}$ phase in Li-inserted LTO by EELS observation. Fig. 2(a) shows the potential profile of the commercial LTO powder (LT-106), revealing the potential plateau around 1.55 V, characteristic of the electrochemical Li insertion reaction in LTO. When the potential reached to cut off range, 1 V as the full charge state, the color of sample powder turned black from white, indicating the electrochemical reduction from Ti^{4+} to Ti^{3+} by Li insertion. We defined this fully-charged powder as Li-LTO. Then we defined the powder that charged at half the time for reaching the fully-charged state as the half-charged one.

Fig. 2(b) shows the ADF (annular dark field)-STEM images of the [110] projection of pristine LTO and Li-LTO samples. The [110] incident is most suitable for observing atoms in different spinel sites directory, because each atomic column corresponds to the alignment of the atoms of the same Wyckoff position. The color spheres in Fig. 2(b) represent atoms in each spinel sites; [$Li_{1/6}Ti_{5/6}$] on octahedral 16d, O on 32e and Li on tetrahedral 8a (octahedral 16c), marked by green, red and yellow, respectively, if we assume the Li-LTO sample corresponds to the $Li_7Ti_5O_{12}$ phase. In the ADF images, white dots represent the atomic positions with the contrast relating to the atomic number. In both the images, regular atomic arrangements of 16d sites of Ti and Li atoms and 32e sites of O atoms were observed with no difference. This is consistent with the conventional view that the occupation of 16d and 32e sites is not changed during the phase transition from $Li_4Ti_5O_{12}$ to $Li_7Ti_5O_{12}$ explained above.

Fig. 2(c) shows the EEL spectra of the pristine LTO and Li-LTO samples. Both the samples have clear peaks at around 61.5 eV, 458 eV and 532 eV, corresponding to the Li-*K*, Ti-*L* and O-*K* edge energy-loss positions, respectively. For the two samples, the feature of the Ti-*L* edge peak is clearly different from each other, indicating the reduction of Ti^{4+} in the Li-LTO sample by electrochemical Li-insertion reaction [25,26]. Of course, there are other differences for the two samples in the height of the Li-*K* edge peak and in the detailed shape of the O-*K* edge peak.

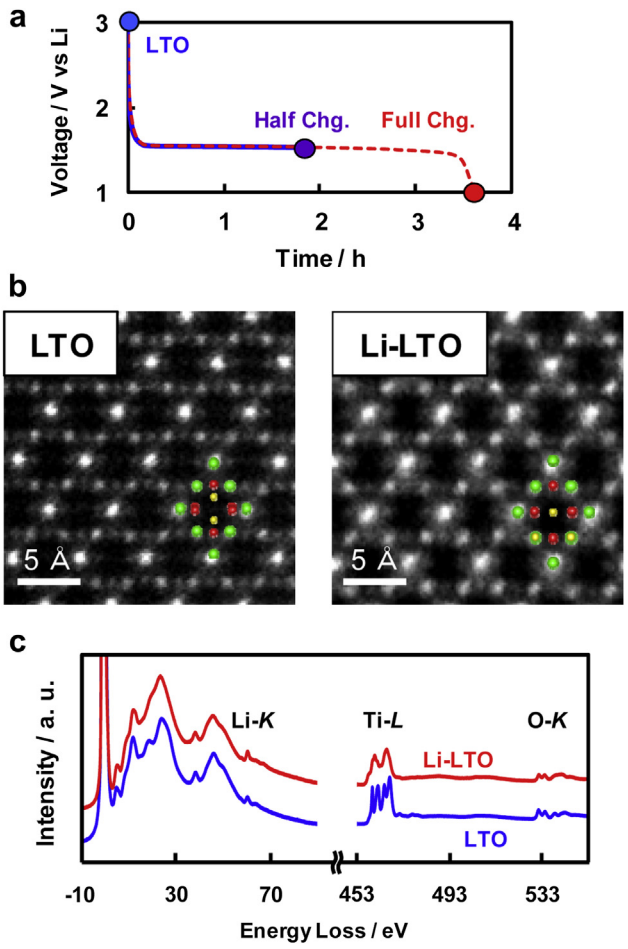

Fig. 2. (a) Charge–discharge potential profile of the commercial $Li_4Ti_5O_{12}$ (LTO) powder sample. The extremely flat voltage around 1.55 V means that the characteristic two-phase reaction is progressing in secondary particles. (b) Typical [110]-projected ADF images of pristine and fully charged LTO (Li-LTO) samples. The green, red and yellow color spheres correspond to 16d sites of Li and Ti atoms, 32e sites of O atoms, and 8a (16c) sites of Li atoms in $Li_4Ti_5O_{12}$ ($Li_7Ti_5O_{12}$), respectively. (c) EEL spectra of LTO and Li-LTO samples, acquired from Li-*K*, Ti-*L* and O-*K* edge energy-loss regions. (For interpretation of the references to color in this figure legend, the reader is referred to the web version of this article.)

The present EEL spectra of the Li-LTO sample clearly shows that a different phase is really formed from the LTO powder by the electrochemical reaction. However, there remains uncertainty that the generated phase is exactly $Li_7Ti_5O_{12}$ or not. Thus here we perform more detailed EELS analyzes of the Li-LTO sample, compared to the pristine LTO sample in the following subsections. Detailed features of the Li-*K* and Ti-*L* edges provide the information of compositions and chemical states of each species, and those of the O-*K* edge provide the information on the local configuration around oxygen atoms.

3.2. Determination of the Li composition in the Li-inserted phase by Li-K edge spectra

The intensity of the Li-*K* peak should depend on the Li composition of Li–Ti–O systems. Fig. 3(a) shows the Li-*K* edge spectra for β-Li_2TiO_3 [27] (A), Li-LTO (B), LTO (C), and rutile-TiO_2 (D). These spectra were acquired by the integration of spectrum imaging data at the area of same relative thickness (t/λ for 0.4–0.6, λ means the

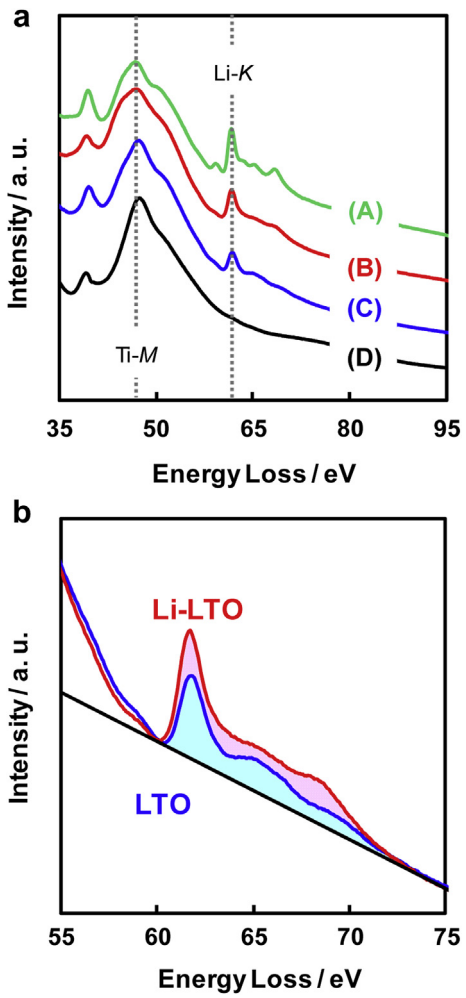

Fig. 3. (a) Li-*K* edge spectra of various lithium titanates; (A) β-Li_2TiO_3, (B) fully Li-inserted LTO (Li-LTO), (C) pristine LTO, and (D) rutile-TiO_2. All the spectra were normalized at zero-loss peak (ZLP) intensity and calibrated at its energy position. (b) Li-*K* edge spectra of LTO and Li-LTO extended from figure (a).

mean free path of electron) and were normalized at zero-loss peak (ZLP) intensity, indicating that the spectra are normalized for the electron dose. The spectra of lithium titanate from (A) to (C) have a clear peak at the same energy position (61.5 eV), identified as the Li-*K* edge peak. The intensity of this peak for Li-LTO (B) is higher than that for LTO (C), indicating the relation of the volume density of lithium atoms. Here, it is difficult to obtain the absolute Li density value for the Li-inserted LTO phase experimentally, because the absolute sample thicknesses were not clearly known. However, we can estimate relative Li density by comparing the signal intensity in these two spectra.

Fig. 3(b) shows the Li-*K* edge spectra of LTO and Li-LTO samples extended from Fig. 3(a). These two spectra are nearly overlapped in each other but the peak height and area are slightly different, indicating the different Li density between these two samples. To acquire the signal intensity, we used the linear background correction, differently from usual power law background correction. This is because the Li-*K* edge slightly overlaps with Ti-*M* and Plasmon loss spectra and the conventional background models are not suitable. The Li volume density of Li-LTO was evaluated as 31.5 (Li atoms nm^{-3}) by comparing the signal intensity of Li-LTO (red area in the web version) with LTO (blue area in the web version) and using a simple estimation value of 18.3 Li atoms nm^{-3} for LTO from the composition and equilibrium volume. This value corresponds to $Li_{6.8}Ti_5O_{12}$ as the chemical composition, because of negligible volume changes in LTO by the Li insertion. This indicates that the formed Li-LTO sample is almost similar to the end member's of Li inserted reaction, $Li_7Ti_5O_{12}$.

3.3. Detailed features of the Ti-L edge spectrum of the Li-inserted phase

In $Li_7Ti_5O_{12}$, 60% of Ti^{4+} ions in LTO should be changed into Ti^{3+}. The oxidation state of Ti can be examined sensitively by the Ti-*L* edge spectrum. Fig. 4(a) shows the Ti-*L* edge spectra of LTO, Li-LTO and Ti_2O_3 samples, respectively. The Ti-*L* edge spectrum of LTO shows four peaks typical of Ti^{4+}, consisting of doublet t_{2g}-e_g splitting of L_2 (higher) and L_3 (lower) edges [28–30]. In the spectrum of a pure Ti^{3+} oxide (Ti_2O_3), there are also two peaks in each L_3 and L_2 edges [25]. However, the partial occupancy of 3*d* electrons in Ti^{3+} greatly decreases the lower peak, making it almost a shoulder in each L_3 and L_2 edges. This is because the present spectra represent the excitation to unoccupied 3*d* states. At the same time, we can see the lowering of the onset energy, which is typical of species with decreased oxidation states.

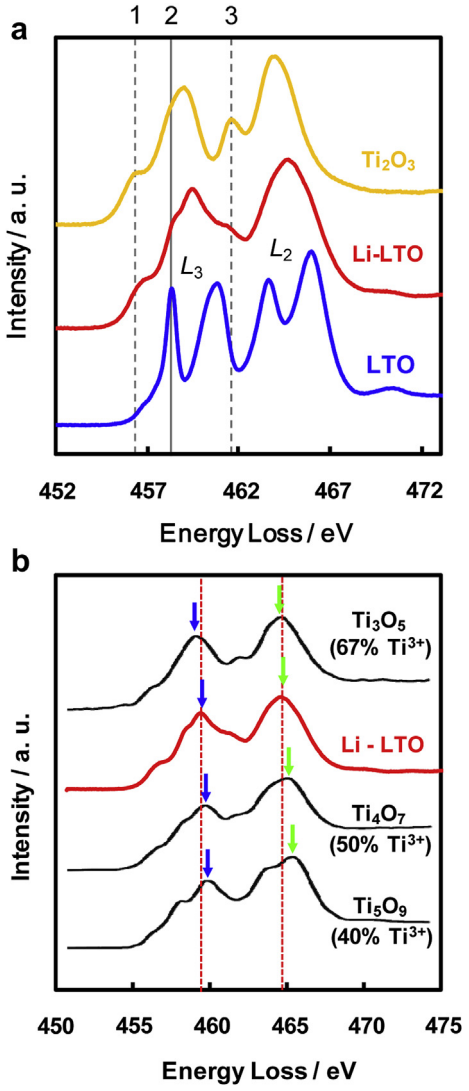

Fig. 4. (a) Ti-*L* edge spectra of LTO, Li-LTO and Ti_2O_3. The spectra of LTO and Ti_2O_3 were calibrated by Ref. [25] and all the spectra were normalized at the L_3 edge peak intensity of LTO. (b) Comparison of the chemical shift of the peak-top positions of various titanium oxides. These spectra except Li-LTO were quoted from Ref. [25].

The feature of the Ti-*L* edge spectrum of Li-LTO is rather similar to the feature of Ti_2O_3 than that of LTO. However, the spectrum of Li-LTO has some differences from that of Ti_2O_3, such as the presence of a shoulder at the energy position 2 and the decrease in the peak height at the energy position 3, compared to Ti_2O_3. These changes in Li-LTO can be understood from the view point of the mixture of the two spectra of LTO and Ti_2O_3. In other words, the Ti-*L* edge spectrum of Li-LTO can be explained as the mixture of Ti^{3+} and Ti^{4+}, which is consistent with the fact that $Li_7Ti_5O_{12}$ as the Li-inserted phase contains both Ti^{3+} and Ti^{4+}.

Fig. 4(b) shows the Ti-*L* edge spectra of several titanium oxides and Li-LTO, containing both Ti^{3+} and Ti^{4+}, where the spectra of Ti_5O_9 (40% Ti^{3+}), Ti_4O_7 (50% Ti^{3+}), Ti_3O_5 (67% Ti^{3+}) are obtained from previous reports [25]. We can see that the energy positions of peak tops of L_2 and L_3 edges marked by allow shift from higher to lower, according to the increase (decrease) of the ratio of Ti^{3+} (Ti^{4+}). The peak top positions of Li-LTO intervene between Ti_4O_7 (50% Ti^{3+}) and Ti_3O_5 (67% Ti^{3+}), which is reasonable if we consider that the ratio of Ti^{3+} in Li-LTO is about 60% just as the $Li_7Ti_5O_{12}$ phase.

3.4. Local structural characterization by the O-K edge spectrum in the Li-inserted phase

We deal with the O-*K* edge spectrum to provide the information on local coordination structure of oxygen atoms, such as configurations and kinds of neighboring cationic species. This is because the spectrum is caused by the transition from the O 1*s* state to the O 2*p* final states in the conduction band, hybridized with valence orbitals of neighboring cationic atoms. During the structural change from $Li_4Ti_5O_{12}$ to $Li_7Ti_5O_{12}$, the spinel frame consisting of Ti and Li atoms on 16d sites and O atoms on 32e sites is fixed, while Li atoms on 8a sites are greatly changed.

Fig. 5(a) shows the present results of the O-*K* edge spectra of LTO, Li-LTO and β-Li_2TiO_3. In all the spectra, two pronounced peaks 1 and 2 originate from transitions to the 2*p* states hybridized with Ti 3*d* orbitals, and the splitting is due to t_{2g}-e_g splitting of the Ti 3*d* levels. The splitting value (shown as Δ_{1-2}) is slightly different among the three systems; 2.5 eV for Li-LTO (Ti^{3+}, Ti^{4+}), and 2.8 eV for LTO and β-Li_2TiO_3 (Ti^{4+}). This tendency is similar to that observed in Ref. [25], where the effects of the changes in valence states and site geometry in Ti_xO_y phases were observed by Ti-*L* and O-*K* edge EEL spectra.

The peaks 3, 4 and 5 in each spectrum should originate from the mixing of the O 2*p* orbitals with *s* and *p* orbitals of Li and Ti atoms [30], and are remarkably dependent on the materials, in contrast to the peaks 1 and 2. The features of these peaks for Li-LTO are similar to those of β-Li_2TiO_3, and quite different from those of LTO. The three materials have the peak 3 commonly. The peak 4 in Li-LTO and β-Li_2TiO_3 is so large to form a continuous peak with the peak 3, while the peak 4 in LTO is only a shoulder of the peak 5. For LTO, the peak 5 is large, while that in Li-LTO and β-Li_2TiO_3 is negligible. The coordination structures of oxygen atoms of LTO, $Li_7Ti_5O_{12}$ and β-Li_2TiO_3 are shown in Fig. 5(b), where $Li_7Ti_5O_{12}$ and β-Li_2TiO_3 have octahedral coordination, and only LTO has tetrahedral coordination. This structural difference should cause the difference in the features of the peaks 4 and 5. β-Li_2TiO_3 has the oxidation state of Ti (Ti^{4+}) similar to LTO, while the peaks 4 and 5 of β-Li_2TiO_3 are similar to those of Li-LTO due to the similar oxygen coordination. In addition, there is a tendency that the peaks 3 and 4 are higher than or match the peaks 1 and 2 in Li-LTO and β-Li_2TiO_3, while the peaks 3, 4 and 5 are not so high compared to the peaks 1 and 2 in LTO. This should be caused by the higher densities of Li—O hybridization due to the higher Li-composition ratio against O in Li-LTO ($Li_7Ti_5O_{12}$) and β-Li_2TiO_3, compared to LTO ($Li_4Ti_5O_{12}$).

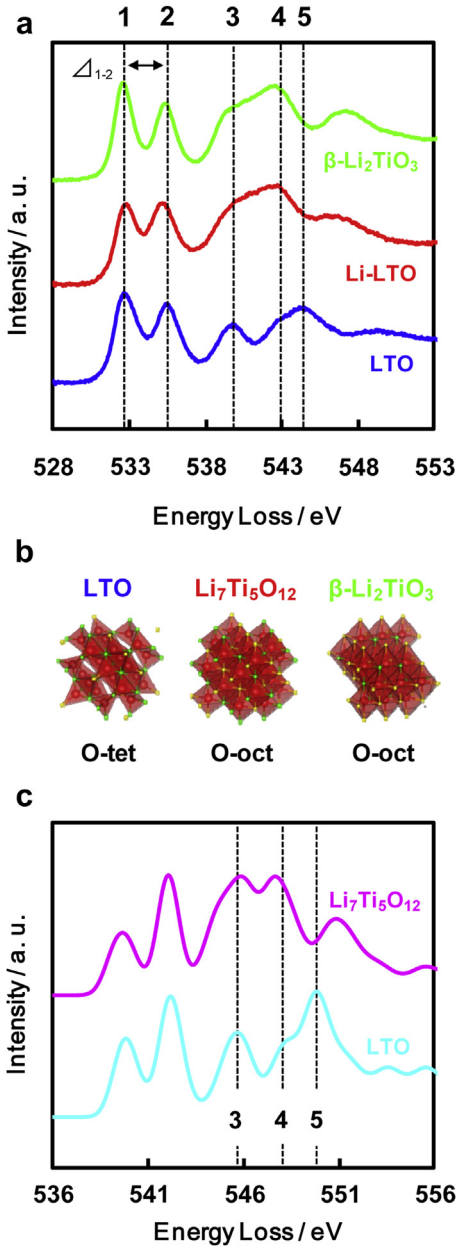

Fig. 5. (a) O-*K* edge spectra of LTO, Li-LTO and β-Li_2TiO_3. All the spectra were calibrated at O-*K* pre-edge peak position and normalized at Ti-L_3 edge intensity which was measured simultaneously. (b) Crystal structures of LTO, $Li_7Ti_5O_{12}$ and β-Li_2TiO_3. Green, red and yellow colored spheres indicate Ti, O and Li atoms, respectively. Each polyhedron shows the oxygen coordination structure in each crystal. (c) Calculated O-*K* edge spectra of LTO and $Li_7Ti_5O_{12}$ by using the PAW-GGA method [31,35]. These spectra were obtained by averaging the spectra of various O sites. (For interpretation of the references to color in this figure legend, the reader is referred to the web version of this article.)

The present consideration is proved by the first principles calculations of the O-*K* edge spectra of LTO and $Li_7Ti_5O_{12}$ [31] by using the projector augmented wave (PAW) method [32,33] within the generalized gradient approximation (GGA) [34]. After determining the crystal structure, the spectrum is obtained by the transition matrix within a dipole approximation for a large supercell containing a core hole [35]. The present scheme has good accuracy as the FLAPW (full potential augmented plane wave) method [36], at least for *K*-edge spectra, and requires relatively small computational efforts, which enables us to deal with complex crystal structures such as LTO. To deal with realistic atomic configurations

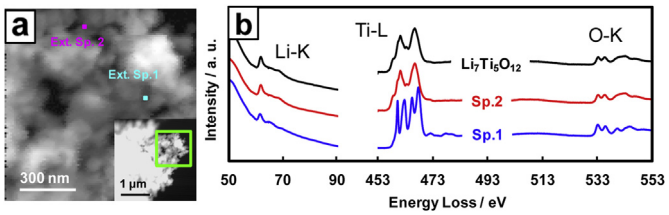

Fig. 6. (a) Spectrum image of a half-charged LTO secondary particle, acquired from a square area of inset. The data was acquired with 103 × 103 pixel resolution at 10 nm pixel steps. (b) Typical EEL spectra of the Li-*K*, Ti-*L* and O-*K* regions, obtained from the positions of Sp. 1 and Sp. 2 in (a). The spectrum of $Li_7Ti_5O_{12}$ from the fully-charged Li-LTO sample is also shown in black solid line.

of LTO and $Li_7Ti_5O_{12}$ where only Li—Ti ratios at 16d sites are known, we adopted large supercells (168 atom and 192 atom cells for LTO and $Li_7Ti_5O_{12}$, respectively) with atomic coordinates decided according to the strategy in Ref. [37]. Results are shown in Fig. 5(c), where the features of the peaks 4 and 5 are completely different between the two phases, similarly to the observed spectra in Fig. 5(a). The comparison between the theoretical and experimental results also suggests that Li-LTO corresponds to $Li_7Ti_5O_{12}$.

3.5. Visualization of the two-phase distribution morphology in the half charged $Li_4Ti_5O_{12}$ secondary particle by STEM—EELS observation

In the above examination, we conclude that the $Li_7Ti_5O_{12}$ phase can be identified by EELS. In this subsection, we investigate the two-phase distribution morphology during the Li-insertion reaction in the LTO powder, by using the information of the EEL spectra of the $Li_4Ti_5O_{12}$ and $Li_7Ti_5O_{12}$ phases. We acquired the spectrum image of the half-charged sample (as shown in Fig. 2(a)). Fig. 6(a) shows the Ti-*L* and Li-*K* edge EEL spectrum image of the half-charged sample, acquired from a square area shown in inset. The white contrast means the intensity of inelastic scattering electrons at 453 eV energy loss, almost indicating the thickness of the sample.

We have found the two places, Sp. 1 and Sp. 2, from which the EEL spectra almost correspond to those of the $Li_4Ti_5O_{12}$ and $Li_7Ti_5O_{12}$ phases, respectively, as shown in Fig. 6(b). The Ti-*L* edge spectrum at Sp. 2 shows two peaks, similarly to the $Li_7Ti_5O_{12}$ phase with the increase of Ti^{3+}, while the Ti-*L* edge spectrum at Sp. 1 shows clear four peaks as LTO with only Ti^{4+}, as discussed in Section 3.3. The intensity of the Li-*K* peak at 61.5 eV for Sp. 2 is higher than that for Sp. 1, consistently with the relation between the two phases. The shapes in the higher energy region in the O-*K* edge spectra also indicate that Sp. 1 and Sp. 2 correspond to the $Li_4Ti_5O_{12}$ and $Li_7Ti_5O_{12}$ phases, respectively, as discussed in Section 3.4. Thus we can make the spectral image of the two-phase distribution based on the spectra at Sp. 1 and Sp. 2.

In order to visualize the two-phase distribution, we have to reconstruct the spectrum images with respect to the differences in each Ti-*L* and Li-*K* edge region. For the Ti-*L* edge region, we applied the multiple linear least squire fitting (MLLS) scheme [38] to obtain the distribution, where the observed spectrum $F(\mathbf{r}_i, \varepsilon)$ at the two dimensional grid point $\mathbf{r}_i$ in the STEM observation is approximated by a linear combination of the two spectra at Sp. 1 ($f_1(\varepsilon)$) and Sp. 2 ($f_2(\varepsilon)$), representing $Li_4Ti_5O_{12}$ and $Li_7Ti_5O_{12}$ respectively, as follows,

$$F(\mathbf{r}_i, \varepsilon) = C_1(\mathbf{r}_i) f_1(\varepsilon) + C_2(\mathbf{r}_i) f_2(\varepsilon) \ldots \quad (2)$$

For each two dimensional grid point $\mathbf{r}_i$, the coefficients $C_1(\mathbf{r}_i)$ and $C_2(\mathbf{r}_i)$ are determined by the least square fitting of the spectra data of the loss energy ε in the Ti-*L* edge region.

Fig. 7(a) shows the spectral image from the data in the Ti-*L* edge region. We can clearly see the red domains of remarkably high components of Sp. 2, meaning the $Li_7Ti_5O_{12}$ phase, with the shapes of primary particles, near the edges of the secondary particle. We can also see the green domains of remarkable high components of Sp. 1, meaning the $Li_4Ti_5O_{12}$ phase, in the other regions. This indicates the presence of both the $Li_7Ti_5O_{12}$ and $Li_4Ti_5O_{12}$ primary particles within the LTO secondary particle. Of course, it seems that the spectra from the middle part of the secondary particle are due to the overlap of the spectra of the two phases.

On the other hand, we can make a spectral image according to the intensity of the Li-*K* edge peak in each spectrum of the two dimensional grid as shown in Fig. 7(b). The intensity was obtained by the integration of the Li-*K* peak from 61 eV to 63 eV after the linear background correction and normalized by the sample thickness. In Fig. 7(b), we can see the domains with remarkably high intensity of the Li-*K* edge peak of red colors, while the domains with relatively low intensity of green colors can be also seen. As discussed in Section 3.2, the intensity corresponds to the Li volume density. The distribution of the domains with different Li volume densities in Fig. 7(b) is clearly correlated to the distribution of the domains with different Ti oxidation states in Fig. 7(a). Thus it can be said that the two kinds of domains correspond to the $Li_7Ti_5O_{12}$ and $Li_4Ti_5O_{12}$ particles, respectively.

From these results, we can conclude that the secondary LTO particle at the half-charged state contains both the $Li_7Ti_5O_{12}$ and $Li_4Ti_5O_{12}$ primary particles. This kind of separate two-phase morphology supports the particle-by-particle reaction mechanism shown in Fig. 1(b).

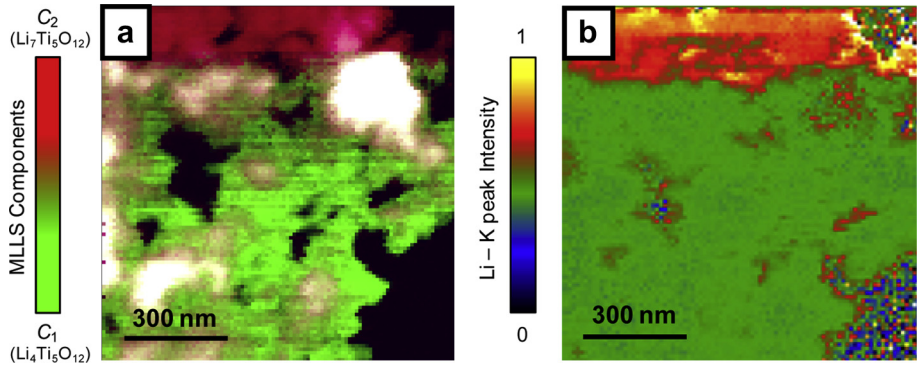

Fig. 7. (a) STEM—EELS spectrum image from the data of the Ti-*L* edge region, representing the distribution of the spectral components of Sp. 1 (green) and Sp. 2 (red) in Fig. 6(b), obtained via the MLLS fitting. White color represents the region of grid points where accurate fitting fails due to large thickness of the sample. (b) STEM—EELS spectrum image of the Li-*K* peak intensity. The color bar shows the linear scale of Li-*K* signal intensity, normalized by the sample thickness. Note that the map has higher intensity values than the Li-rich region, only partially by numerical errors due to the thickness normalization at vacant regions. (For interpretation of the references to color in this figure legend, the reader is referred to the web version of this article.)

3.6. Electrochemical reaction mechanism in LTO secondary particles

The present results indicate that the particle-by-particle reaction really occurs in secondary particles of LTO during usual electrochemical Li-insertion reaction, where the rate determining process within the secondary particle exists not inside a primary particle but at the boundary between primary particles.

The reaction distribution in the secondary particle should be regulated by several factors, and both the electron conduction and Li-ion diffusion should be important. For the electron conduction, particle boundaries should be important due to their low conductivity as contact resistance between primary particles. For the Li-ion diffusion process, the progress of the Li-insertion should be more rapid inside each particle than across the boundary, and there seems to be no preferential diffusion along the boundaries between primary particles.

Experimentally, the Li-ion transfer at the electrode/electrolyte interfaces seems to dominate the total reaction rate of the battery cell as the large activation barrier for the desolvation of lithium ions [39–41]. However, the details of the reaction process inside the electrode are also of great importance so as to attain the stable and high rate performance of the battery electrode.

The present analysis has clarified the importance of the progress of the electrochemical reaction across the boundary between primary particles in actual LTO powder, and the present knowledge should be useful for the powder design of actual LTO materials. At present, we cannot decide the key factor to dominate the reaction diffusion across the particle boundaries. However, here we suggest that the surface or boundary modification of primary particles might be effective than the bulk modification.

Of course, it is necessary to investigate the boundary structures between primary particles and the structures between $Li_7Ti_5O_{12}$ and $Li_4Ti_5O_{12}$ primary particles in a secondary particle, which should be investigated in the near future. The particle-by-particle reaction mechanism means that the reaction resistance at boundaries is higher than that in the each primary particle. However, it is also important to understand the detailed process and rate of the Li-insertion reaction inside a primary particle, namely a LTO bulk crystal, where we have to reveal the structure and stability of the two-phase boundaries, the growth and extension of the Li-inserted phase, and the Li diffusion.

4. Conclusion

In order to investigate the two-phase distribution in commercially-used LTO ($Li_4Ti_5O_{12}$) powder during the Li-insertion process, we have applied the STEM–EELS observation to LTO secondary particles consisting of single crystalline primary particles of nanometer sizes. First, we have examined whether fully-charged Li-inserted LTO (Li-LTO) corresponds to the $Li_7Ti_5O_{12}$ phase or not. By the Li-*K* edge peak intensity, the composition of the Li-LTO sample was estimated as $Li_{6.8}Ti_5O_{12}$, almost similar to $Li_7Ti_5O_{12}$. About the Ti-*L* edge feature, the splitting feature indicates the mixture of Ti^{3+} and Ti^{4+}, and the degree of chemical shift of the peak-top positions indicates the composition of Ti^{3+} of nearly 60%, supporting that the Li-LTO sample is $Li_7Ti_5O_{12}$. The O-*K* edge spectrum reveals the typical feature of octahedral coordination of oxygen, similarly to $Li_7Ti_5O_{12}$, and quite differently from LTO. In addition, the O-*K* edge spectra of LTO and Li-LTO are well reproduced by the first-principles calculations for $Li_4Ti_5O_{12}$ and $Li_7Ti_5O_{12}$ crystals, suggesting that the Li-LTO phase is $Li_7Ti_5O_{12}$. Second, we have examined the two-phase distribution in the half-charged LTO sample by the STEM–EELS spectrum imaging scheme. The spectrum images from the Ti-*L* edge feature and from the Li-*K* edge peak intensity have clarified that the two phases of $Li_4Ti_5O_{12}$ and $Li_7Ti_5O_{12}$ exist separately along the shapes of primary particles in a secondary particle, suggesting the particle-by-particle reaction mechanism. Thus the reaction rate should be dominated by the resistance of the progress of the Li-insertion reaction across the boundaries between primary particles.

Acknowledgment

The authors thank Dr. Noboru Taguchi for EELS data analysis and valuable discussion. This work was supported by the Japan Society for the Promotion of Science (JSPS Grant-in-Aid for Scientific Research (B) 22360276).

References

[1] D. Aurbach, E. Zinigrad, Y. Cohen, H. Teller, Solid State Ion. 148 (2002) 405–416.
[2] R.M. Dell, Solid State Ion. 134 (2000) 139–158.
[3] J.-M. Tarascon, M. Armand, Nature 414 (2001) 359–367.
[4] A. Deschanvres, B. Raveau, Z. Sekkal, Mater. Res. Bull. 6 (1971) 699–704.
[5] K.M. Colbow, J.R. Dahn, R.R. Haering, J. Power Sources 26 (1989) 397–402.
[6] E. Ferg, R.J. Gummov, A. de Kock, M.M. Thackeray, J. Electrochem. Soc. 141 (1994) L147–L150.
[7] T. Ohzuku, A. Ueda, N. Yamamoto, J. Electrochem. Soc. 142 (1995) 1431–1435.
[8] N. Takami, H. Inagaki, T. Morita, Toshiba Rev. 61 (2006) 6–10.
[9] N. Takami, H. Inagaki, T. Kishi, Y. Harada, Y. Fujita, H. Hoshina, J. Electrochem. Soc. 156 (2009) A128–A132.
[10] S. Scharner, W. Weppner, P. Schmid-Beurmann, J. Electrochem. Soc. 146 (1999) 857–861.
[11] K. Ariyoshi, R. Yamato, T. Ohzuku, Electrochim. Acta 51 (2005) 1125–1129.
[12] N. Takami, K. Hoshina, H. Inagaki, J. Electrochem. Soc. 158 (2011) A725–A730.
[13] F. Ronci, P. Reale, B. Scrosati, S. Panero, V. Rossi Albertini, P. Perfetti, M. di Michiel, J.M. Merino, J. Phys. Chem. B 106 (2002) 3082–3086.
[14] H. Ge, N. Li, D. Li, C. Dai, D. Wang, J. Phys. Chem. C 113 (2009) 6324–6326.
[15] K. Kataoka, Y. Takahashi, N. Kijima, H. Hayakawa, J. Akimoto, K. Oshima, Solid State Ion. 180 (2009) 631–635.
[16] L. Aldon, P. Kubiak, M. Womes, J.C. Jumas, J. Olivier-Fourcade, J.L. Tirado, J.I. Corredor, C. Pérez Vicente, Chem. Mater. 16 (2004) 5721–5725.
[17] J.-F. Colin, V. Godbole, P. Novák, Electrochem. Commun. 12 (2010) 804–807.
[18] P.E. Batson, Ultramicroscopy 59 (1995) 63–70.
[19] C. Colliex, Nature 450 (2007) 622–623.
[20] L. Laffont, C. Delacourt, P. Gibot, M.Y. Wu, P. Kooyman, C. Masquelier, J.-M. Tarascon, Chem. Mater. 18 (2006) 5520–5529.
[21] J. Kikkawa, T. Akita, M. Tabuchi, M. Shikano, K. Tatsumi, M. Kohyama, Electrochem. Solid-State Lett. 11 (2008) A183–A186.
[22] J. Kikkawa, T. Akita, M. Tabuchi, M. Shikano, K. Tatsumi, M. Kohyama, Appl. Phys. Lett. 91 (2007) 054103.
[23] M. Kitta, T. Akita, Y. Maeda, M. Kohyama, Langmuir 28 (2012) 12384–12392.
[24] M. Kitta, T. Akita, Y. Maeda, M. Kohyama, Appl. Surf. Sci. 258 (2012) 3147–3151.
[25] E. Stoyanov, F. Langenhorst, G. Steinle-Neumann, Am. Mineral. 92 (2007) 577–586.
[26] G. Radtke, S. Lazar, G.A. Botton, Phys. Rev. B 74 (2006) 155117.
[27] K. Kataoka, Y. Takahashi, N. Kijima, H. Nagai, J. Akimoto, Y. Idemoto, K.-I. Ohshima, Mater. Res. Bull. 44 (2009) 168–172.
[28] R.D. Leapman, L.A. Grunes, P.L. Fejes, Phys. Rev. B 26 (1982) 614–636.
[29] C. Mitterbauer, G. Kothleitner, W. Grogger, H. Zandbergen, B. Freitag, P. Tiemeijer, F. Hofer, Ultramicroscopy 96 (2003) 469–480.
[30] P.-E. Lippens, M. Womes, P. Kubiak, J.-C. Jumas, J. Olivier-Fourcade, Solid State Sci. 6 (2004) 161–166.
[31] S. Tanaka, M. Kitta, T. Tamura, T. Akita, Y. Maeda, M. Kohyama, J. Phys. D 45 (2012) 494004.
[32] P.E. Blöchl, Phys. Rev. B 50 (1994) 17953–17979.
[33] G. Kresse, D. Joubert, Phys. Rev. B 59 (1999) 1758–1775.
[34] J.P. Perdew, K. Burke, M. Ernzerhof, Phys. Rev. Lett. 77 (1996) 3865–3868.
[35] T. Tamura, S. Tanaka, M. Kohyama, Phys. Rev. B 85 (2012) 205210.
[36] C. Hebert, Micron 38 (2007) 12–28.
[37] C.Y. Ouyang, Z.Y. Zhong, M.S. Lei, Electrochem. Commun. 9 (2007) 1107–1112.
[38] A. Maigne, R.D. Twesten, J. Electron. Microsc. 58 (2009) 99–109.
[39] I. Yamada, T. Abe, Y. Iriyama, Z. Ogumi, Electrochem. Commun. 5 (2003) 502–505.
[40] T. Abe, H. Fukuda, Y. Iriyama, Z. Ogumi, J. Electrochem. Soc. 151 (2004) A1120–A1123.
[41] T. Doi, Y. Iriyama, T. Abe, Z. Ogumi, Anal. Chem. 77 (2005) 1696–1700.